AFRL-AFOSR-JP-TR-2018-0039

Mach 6-8 Scramjet Combustion Experiments using Hydrocarbon Fuel

Michael Kevin Smart
THE UNIVERSITY OF QUEENSLAND

02/01/2018
Final Report

Air Force Research Laboratory
AF Office Of Scientific Research (AFOSR)/ IOA
Arlington, Virginia 22203
Air Force Materiel Command

REPORT DOCUMENTATION PAGE

Form Approved
OMB No. 0704-0188

1. REPORT DATE *(DD-MM-YYYY)*	2. REPORT TYPE	3. DATES COVERED *(From - To)*
16-05-2018	Final	28 Sep 2015 to 27 Sep 2017

4. TITLE AND SUBTITLE
Mach 6-8 Scramjet Combustion Experiments using Hydrocarbon Fuel

5a. CONTRACT NUMBER

5b. GRANT NUMBER
FA2386-15-1-4093

5c. PROGRAM ELEMENT NUMBER
61102F

6. AUTHOR(S)
Michael Kevin Smart

5d. PROJECT NUMBER

5e. TASK NUMBER

5f. WORK UNIT NUMBER

7. PERFORMING ORGANIZATION NAME(S) AND ADDRESS(ES)
THE UNIVERSITY OF QUEENSLAND
UNIVERSITY OF QUEENSLAND
BRISBANE, 4072 AU

8. PERFORMING ORGANIZATION REPORT NUMBER

9. SPONSORING/MONITORING AGENCY NAME(S) AND ADDRESS(ES)
AOARD
UNIT 45002
APO AP 96338-5002

10. SPONSOR/MONITOR'S ACRONYM(S)
AFRL/AFOSR IOA

11. SPONSOR/MONITOR'S REPORT NUMBER(S)
AFRL-AFOSR-JP-TR-2018-0039

12. DISTRIBUTION/AVAILABILITY STATEMENT
A DISTRIBUTION UNLIMITED: PB Public Release

13. SUPPLEMENTARY NOTES

14. ABSTRACT
The PI for this grant has been very successful. The final report for this grant described supersonic combustion of hydrocarbon fuels at representative scramjet conditions using a cavity combustor using fuelmixtures that are similar in composition to thermally cracked liquid hydrocarbons. These experiments completed include the full threedimensional aspects of a proper scramjet internal flow path. This work also leveraged inhouse expertise in CFD simulations to identify the main fluidmechanic structures that are responsible for the process of mixing and ignition in these combustors. To date, 1 peer reviewed paper and 2 conference papers resulted from this award.

15. SUBJECT TERMS
AOARD, scramjet, hydrocarbon

16. SECURITY CLASSIFICATION OF:			17. LIMITATION OF ABSTRACT	18. NUMBER OF PAGES	19a. NAME OF RESPONSIBLE PERSON
a. REPORT	b. ABSTRACT	c. THIS PAGE			CHEN, JERMONT
Unclassified	Unclassified	Unclassified	SAR	32	19b. TELEPHONE NUMBER *(Include area code)* 315-227-7007

Standard Form 298 (Rev. 8/98)
Prescribed by ANSI Std. Z39.18

Final Report
Mach 6-8 Scramjet Combustion Experiments using Hydrocarbon Fuel

Professor Michael K. Smart
Chair of Hypersonic Propulsion
The University of Queensland
m.smart@uq.edu.au

Dr. Vincent Wheatley
Senior Lecturer
The University of Queensland
v.wheatley@uq.edu.au

Dr. Anand Veeraragavan
Senior Lecturer
The University of Queensland
anandv@uq.edu.au

Executive Summary

Gaseous hydrogen has typically been the fuel of choice for scramjets operating at speeds greater than Mach 7. This is because of its high specific energy content, as well as its fast reaction characteristics in air. The disadvantage of hydrogen is its low density, which is a particular problem for small vehicles with significant internal volume constraints. The current project is investigating the use of gaseous hydrocarbon fuels for: 1) a 3D scramjet above Mach 7 and 2) a canonical axisymmetric isolator/combustor at Mach 6-8. The T4 shock tunnel at UQ, which is capable of producing flows in the Mach number range of 4 – 12, is being used for these experiments.

The objective of the first exercise is to continue the demonstration of supersonic combustion of hydrocarbon fuels at representative scramjet conditions using a cavity combustor using fuel-mixtures that are similar in composition to thermally cracked liquid hydrocarbons. These experiments include the full three-dimensional aspects of a proper scramjet internal flow path. This is complementary to the intended fundamental studies (objective 2) in the axisymmetric combustor experiments in which only the core of the facility flow is ingested in a simplified geometry. The axisymmetric arrangement lends itself well to fundamental exploration of fuel-air mixing, ignition and flame propagation via advanced laser diagnostics such as PLIF, as employed in this study. In parallel to these experiments, this work also leveraged in-house expertise in CFD simulations to identify the main fluid-mechanic structures that are responsible for the process of mixing and ignition in these combustors.

As well as Professor Smart, Dr Wheatley, and Dr. Veeraragavan the participants were:

- Mr Zac Denman – PhD student (combustion: graduated in 2017)
- Mr Michael Roberts – PhD student (fuel system: axisymmetric combustor experiments)
- Mr Sam Grieve – T4 tunnel research engineer (axisymmetric combustor design)

Publications to date:

1. Denman, Z. J., Chan, W. Y., Brieschenk, S., Veeraragavan, A., Wheatley, V., & Smart, M. K. (2016). Ignition Experiments of Hydrocarbons in a Mach 8 Shape-Transitioning Scramjet Engine. Journal of Propulsion and Power, 32(6), 1462-1471.

2. Z. J. Denman, V. Wheatley, M. K. Smart and A. Veeraragavan, "Fuel Injection and Mixing in a Mach 8 Hydrocarbon-Fuelled Scramjet", 20th Australasian Fluid Mechanics Conference, Perth, Australia, 5 – 8 December 2016.

3. Z. J. Denman, V. Wheatley, M. K. Smart and A. Veeraragavan (2017), "Supersonic Combustion of Hydrocarbons in a Shape-Transitioning Hypersonic Engine", Proceedings of the Combustion Institute, 36 (2), 2883-2891.

1. Introduction

Supersonic combustion ramjets (scramjets) are air-breathing engines in which combustion occurs at supersonic speeds. Since the flow remains supersonic, the residence time of the flow within scramjet engines operating beyond Mach 7 is usually on the order of a millisecond. Within this limited residence time available to the flow: fuel injection, fuel-air mixing, ignition, and combustion must occur.

This low residence time for such high-speed engines necessitates having a fuel with a short ignition delay time. Alongside this, a fuel with high energy per unit-mass is required in order to maximize specific impulse [2]. These desired characteristics have led to gaseous hydrogen typically being the fuel of choice for scramjets operating at speeds greater than Mach 7. The low energy per unit volume of gaseous hydrogen, however, is a significant problem for small vehicles with internal volume constraints, in addition to the difficulties associated with its storage and handling. This necessitates research into other fuels in the supersonic combustion regime. Low-order hydrocarbon fuels, such as ethylene and methane, both have much greater energy per unit volume as well as the advantage of easier handling and storage [1]. Table 1 highlights the differences in the energy densities per unit mass and per unit volume for the low-order hydrocarbons considered, liquid kerosene (a practical fuel) as well as hydrogen.

Table 1: Energy properties of low-order hydrocarbons and hydrogen [3]

Fuel	Energy/Mass (MJ/kg)	Energy/Volume (MJ/L)	STP Density (kg/m^3)
Hydrogen	116.7	8.2	71
Methane	50.0	20.8	424
Ethylene	47.2	26.8	568
Liq. Kerosene	46.2	38.4	830

While their energy per unit volume and handling requirements are favourable, low-order hydrocarbons have much greater ignition delay times than hydrogen [4], which is shown graphically in Figure 1. This implies that in order to utilise hydrocarbon fuels, we would require innovations in the combustor design that reduces the ignition time delay or locally increases the residence time in order to achieve robust ignition and complete combustion.

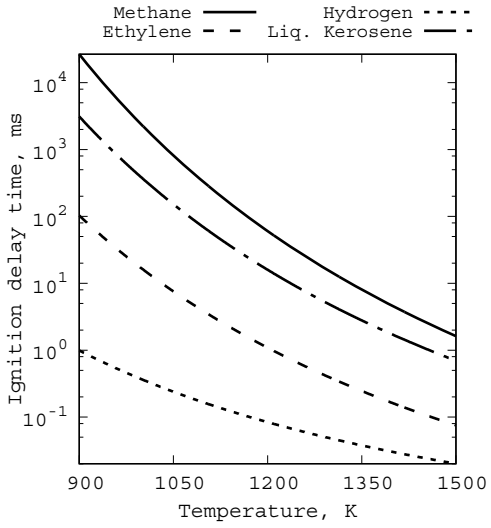

Figure 1: Ignition time delay of different fuels vs temperature.

The current study investigated the use of gaseous hydrocarbons (methane, ethylene and their mixtures) as a fuel for: 1) a Mach 8 scramjet and 2) an axisymmetric combustor operating in a "cookie-cutter" mode wherein only the core of the flow produced in the test facility is ingested by the model. The scramjet tests serve to further demonstrate supersonic combustion of mixtures of methane/ethylene, that are thought to be similar in ignition characteristics to thermally cracked liquid hydrocarbons as proposed in the HIFiRE 2 test [5], in a full, three-dimensional, representative scramjet internal flowpath.

These tests were performed at the University of Queensland's T4 shock tunnel [6]. The inlet geometry of the scramjet is based on the Rectangular-to-Elliptical Shape Transition (REST) configuration of Smart [7]. This fixed geometry, mixed-compression configuration, transitions smoothly from a quasi-rectangular capture shape to an elliptical throat. In combination with a divergent elliptical combustion chamber, REST inlets have been shown to produce a useful flowpath for hypersonic applications [8]. This engine was fitted with a cavity combustor in our previous grant (RESTC engine) that successfully demonstrated supersonic combustion of ethylene at a flight Mach number of 7.3 [1].

In parallel, the fundamental aspects of the fuel-air mixing and ignition process were investigated in a canonical axisymmetric configuration. These experiments utilised the UQ planar-laser-induced-fluorescence (PLIF) system to image the exhaust plumes. The combustion process was visualized using OH-PLIF visualisation performed at a number of streamwise stations. Positioning the visualization plane close to the combustor exit allowed the captured images to accurately represent the flow at that station. This allowed an extensive investigation of the plume and the level of mixing and penetration of fuel jets, flame propagation and extinction. The multi-dimensional visualizations of a key radical in the combustion process provides invaluable validation data for future reacting simulations. Experiments were conducted with gaseous ethylene.

Both experimental works were complemented by the simulations necessary for the design of the experimental models, as well as to shed light on the internal flow features that may not be fully captured by the experimental measurements (particularly in the three-dimensional scramjet testing with no visualisation capabilities).

2. RESTC Engine Studies of Hydrocarbon Mixtures: Experiments and non-reacting mixing simulations

2.1 Experimental Investigations

In this work, we aimed to utilise the Mach 8 rectangular-to-elliptical-shape-transitioning engine with a cavity combustor (RESTC) to further investigate ignition of hydrocarbon fuel mixtures. Figure 2, shows the details of the RESTC engine.

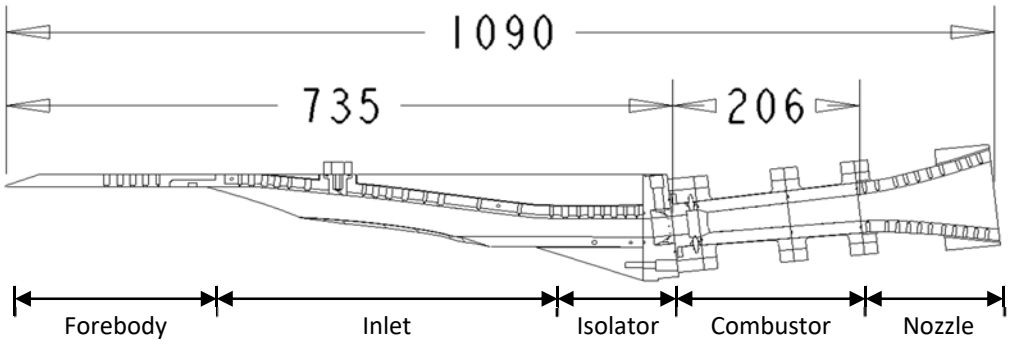

(a) Schematic of Mach 8 REST engine with cavity installed in combustor

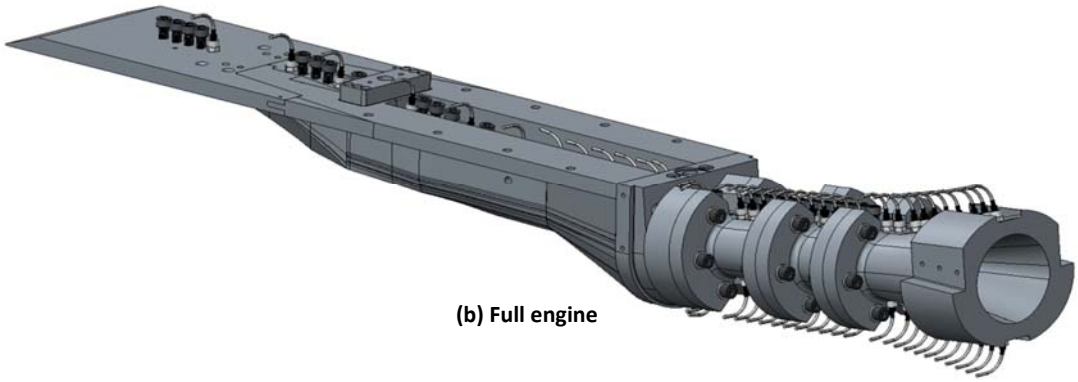

(b) Full engine

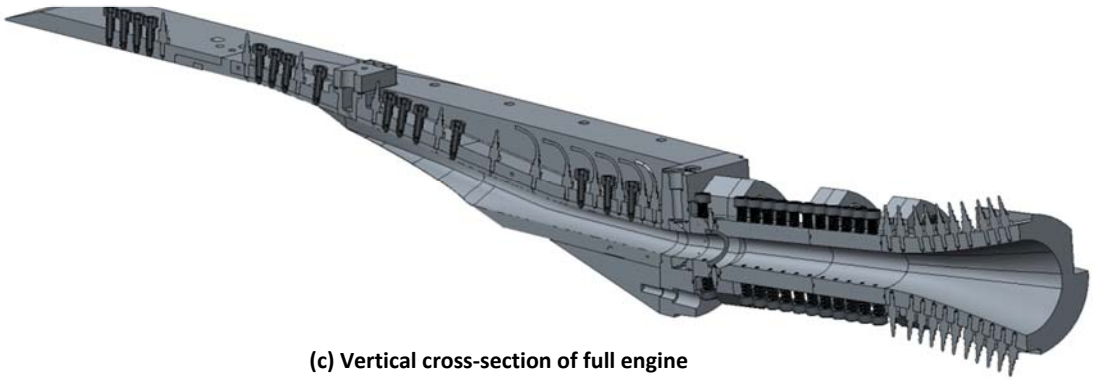

(c) Vertical cross-section of full engine

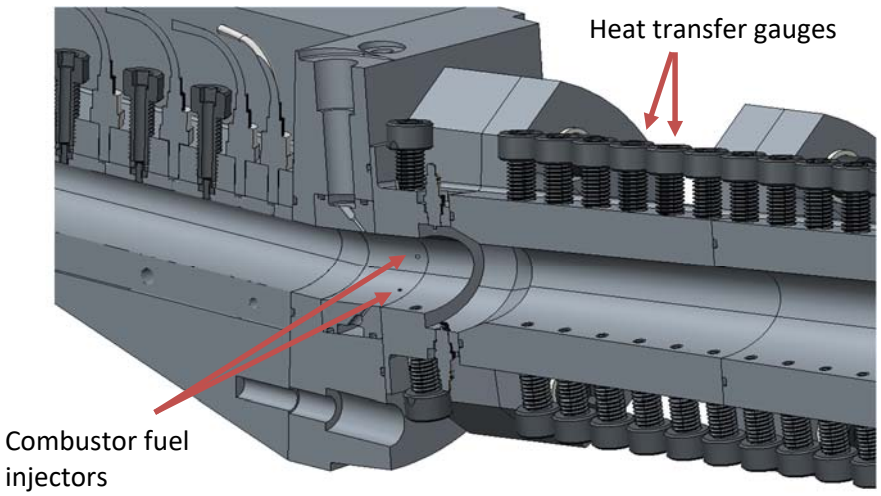

(d) Zoomed view of vertical cross-section showing cavity (pressure transducers are on opposite side of vertical plane)

Figure 2: Schematic and computer-aided design images of modified Mach 8 REST engine

The design of the cavity combustor for the REST engine and the experimental results showcasing a world-first demonstration of ignition of ethylene in a full representative, scramjet engine flowpath were supported by our previous AOARD grant. This cavity design has been fully reported at the 19th AIAA Space Planes Conference [9], while the detailed supersonic combustion experimental results are published in the Journal of Propulsion and Power [1]. In the present work, we employed this same engine to test with a 36% methane and 64% ethylene mixture which follows the fuel choice of the HIFiRE 2 scramjet test [5]. The objective was to investigate if such fuel-mixtures, that are believed to be possess representative ignition characteristics of a thermally cracked liquid hydrocarbon fuel [5], can be ignited above Mach 7 using the cavity combustor.

The test conditions are presented in table 2. The conditions correspond to a Mach 7.3 flight condition.

Table 2: Test conditions for the experiments in the T4 shock tunnel.

Nozzle-supply conditions			Derived freestream conditions					Flight conditions		
p_s	T_s	H_s	p_e	T_e	u_e	M_e	γ_e	M_f	h_f	q_f
MPa	K	MJ/kg	kPa	K	m/s	–	–	–	km	kPa
20.8	2500	2.65	1900	231	2330	7.64	1.40	7.32	28.7	53.5

The RESTC engine is equipped with fuel injectors (locations indicated via vertical black lines in Figure 3) at both the entrance of the inlet as well as just upstream of the cavity combustor. In the first sequence of tests, fuel was only injected at the combustor location to mimic direct-connect combustor experiments. The results of this test are shown in Figure 2. For the equivalence ratios (ϕ) reported in the legend, the subscript "I" refers to the inlet injection and the subscript "C" refers to the combustor injection. The figure reports normalised pressure data (with respect to the free-stream static pressure) and a schematic sketch of the engine is provided over the figure for reference. As can be seen, ϕ_I has been maintained at zero for all of the cases in order to simulate direct-connect like experiments. The sequence of numbers ahead of each case is the shot number corresponding to the shot fired in the T4 shock tunnel to get that dataset. The figure shows four data sets. First, a shot where no fuel was injected (open black squares) to form the baseline. Second and third, shots where the combustor injected equivalence ratio (ϕ_C) was 0.6 (red squares) and 0.8 (blue circles) respectively. And, finally a shot where the test gas was replaced with nitrogen instead of air but with fuel injection on (green triangles), and is denoted the "combustion-suppressed" case. As can be seen from the figure, there is very little difference between the baseline case and the other three cases. This indicates that supersonic combustion was not achieved in these experiments. A small difference in pressure (on both the body and the cowl sides) can be discerned between the baseline case and the three other cases, just downstream of the combustor fuel injection location. Since, the combustion-suppressed case also saw a similar pressure rise compared to the two shots in which air was the test gas with different equivalent ratios, it can be concluded that there was definitely no ignition or supersonic combustion occurring here.

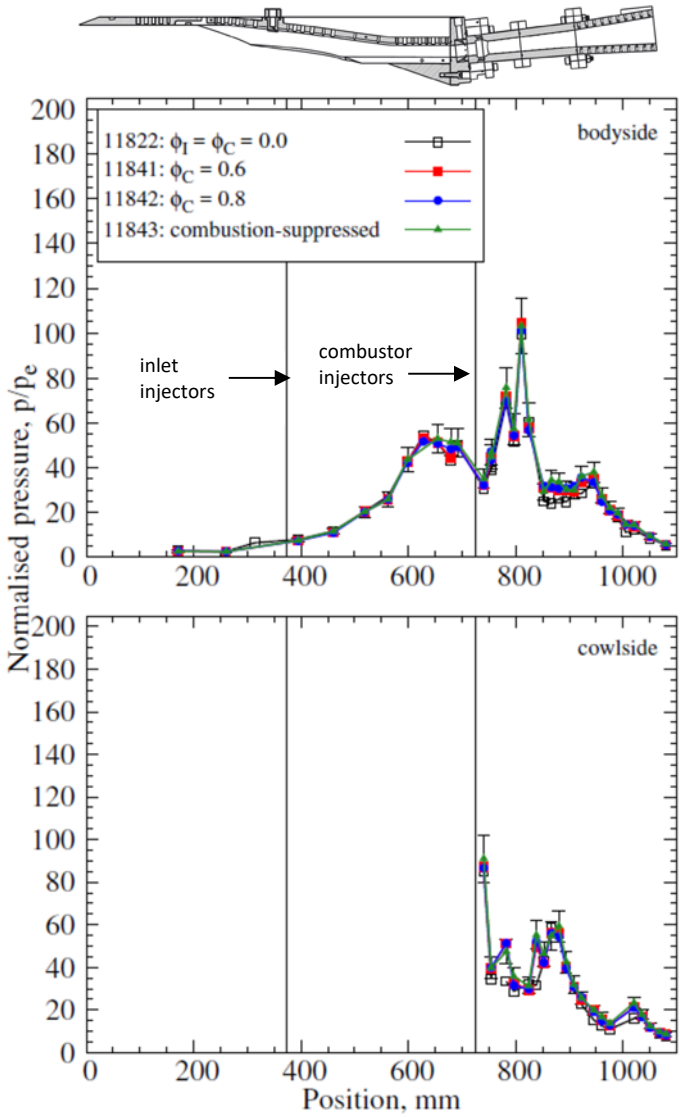

Figure 3: RESTC experimental results for fuel injected via only the combustor injectors.

In the second set of experiments, we attempted to utilise the option of inlet injection to improve the fuel-air mixing and potentially achieve ignition and supersonic combustion. These are reported below in Figure 4. For the test case of interest (red squares), the inlet injection equivalence ratio (ϕ_I) was maintained at 0.3, while the combustor location was fuelled with an equivalence ration (ϕ_C) of 0.6. As before, there is no evidence of supersonic combustion as the small pressure rise noted in comparison to the baseline (no fuel injection case, open black squares) case coincides with that seen for the combustion suppressed (blue circles) case. Therefore, the inlet injection option also failed to ignite and burn this fuel mixture.

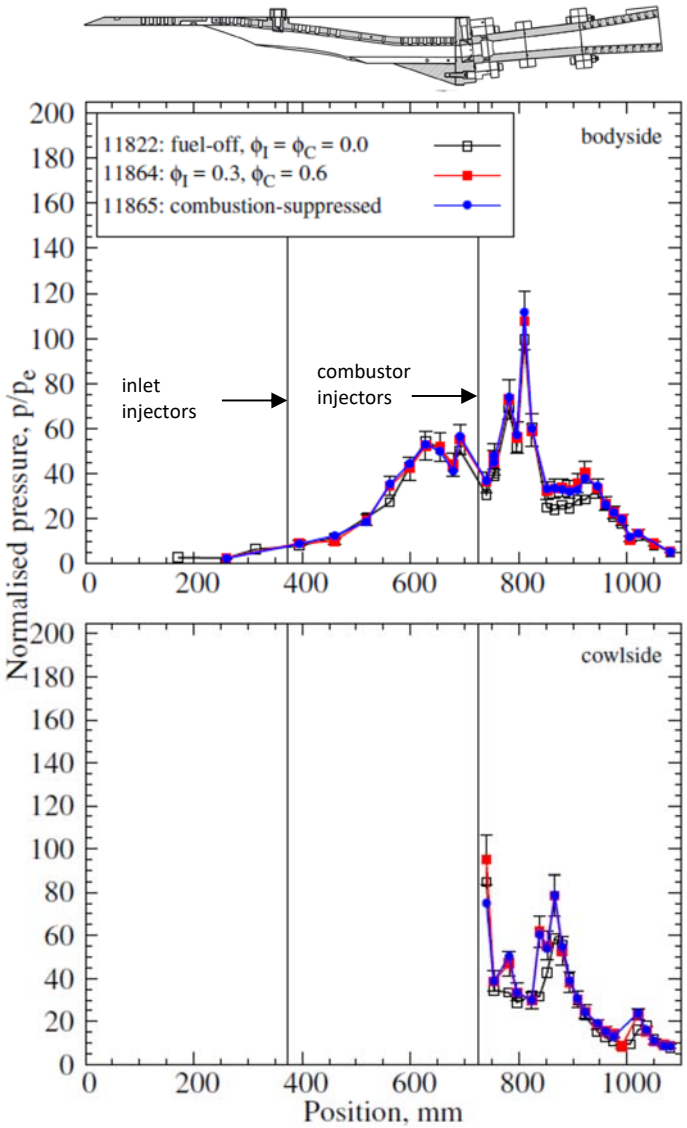

Figure 4: RESTC experimental results for hydrocarbon fuel injected via both the inlet and the combustor injectors.

Finally, we conducted a set of experiments in which the inlet fuel was replaced with hydrogen. As demonstrated in our previous work, this allowed for the inlet injected hydrogen to have a sufficient residence time to mix and ignite close to the start of the combustor portion of the engine. Our aim was to utilise this to our advantage to ignite the hard to ignite mixture of 36% methane + 64% ethylene. The initial tests injected hydrogen with an equivalence ratio (ϕ_I) of 0.3, while maintaining the combustor injection equivalence ratio (ϕ_C) of the methane/ethylene mixture at 0.6. The results of this test are reported in Figure 5. The experiments were conducted with a careful sequential choice of fuel injection in order to isolate and demonstrate that supersonic combustion of this fuel-mixture.

First, the baseline shot was obtained where no fuel was injected (black squares). In the next experiment, the inlet fuel (hydrogen) was turned on while no fuel was injected in the combustor (red squares). It can be seen that this resulted in a rapid mixing and ignition at approximately 600 mm downstream of the inlet injector, with a pressure peak near the combustor injector location. Since no further fuel was added at the combustor injector location for this shot, the pressure then drops sharply as flow moves through the combustor and nozzle. This is due to the inlet injected hydrogen completely burning and no further heat addition occurring to cause additional pressure rise in the remainder of

the flow path. The next experiment had both the inlet hydrogen injection and the combustor injection of ethylene (blue circles). It can be seen that again the inlet injected hydrogen burns through the isolator up to the combustor location. This results in the sustenance of the initial high pressure from the combustion of the inlet injected hydrogen through the remainder of the flow path as the hydrocarbon fuel-mixture now ignites and burns thus contributing further to the heat addition.

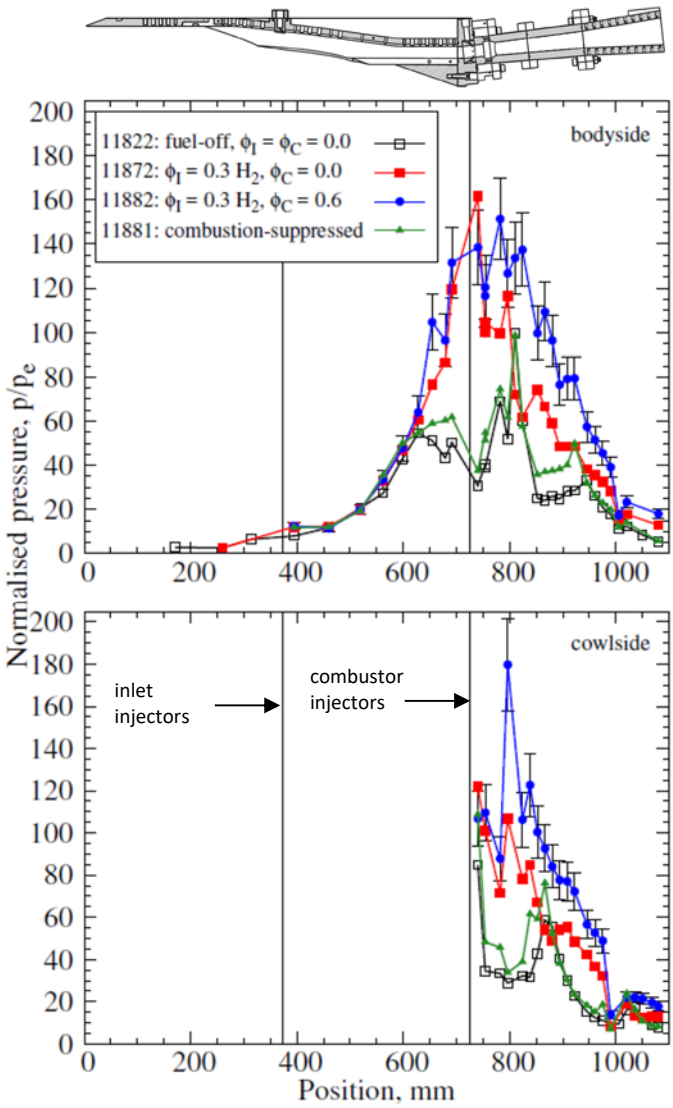

Figure 5: RESTC experimental results for hydrogen injected at inlet (ϕ_I = 0.3) and hydrocarbon fuel injected at the combustor injectors (ϕ_C = 0.6).

The asymmetric flow entering the combustor from the REST inlet results in a combustion flowfield that is also inherently asymmetric. The bodyside of the engine exhibits a gradual pressure increase, culminating at the combustor injection location. This pressure rise is sustained following the ignition of the combustor injected surrogate fuel. However, the pressure distribution on the cowlside of the engine shows a much different trend. The first pressure measurement on the cowlside of the engine (x = 740 mm), which is post combustor injection, shows a much smaller pressure rise due to the lack of a hydrogen pilot on this side of the engine. The pressure peak at this location is due to the shocks that are in the vicinity of that sensor. Both the reflected cowl-closure shock and the shock generated by the six degree bend are present in that region of the engine. The pressure then drops due to the

next transducer being positioned within the cavity flameholder, i.e., behind a rearward facing step. The second, larger rise in pressure on the cowlside of the engine (x = 800 mm) in the piloted experiment is due to the ignition of the surrogate fuel.

The inlet injection of hydrogen was halved in the next set of experiments presented in Figure 6. In spite of this significant reduction in inlet injection of hydrogen, the same ignition and burning processes occur. The figure clearly shows this occurring, however, the peak pressures reached in the flow path are significantly lower. The decrease in hydrogen leads to a reduction in the pressure seen at the combustor entrance. This results in less vigorous combustion of the surrogate fuel throughout the combustor. Therefore, while even a small hydrogen pilot helps in attaining ignition of the surrogate fuel, ideally a stronger pilot is preferred to improve the ignition and subsequent robust combustion of the surrogate fuel. These results were presented at the International Combustion Symposium in Seoul, South Korea (2016) and accepted to the Proceedings of the Combustion Institute [10].

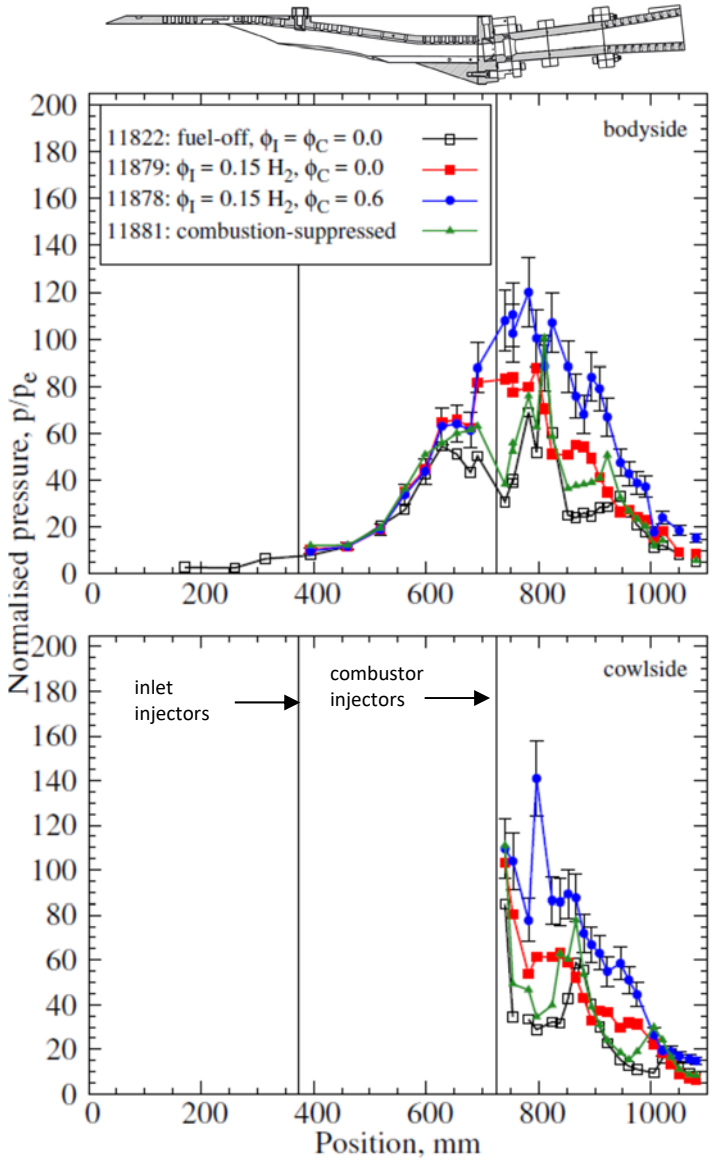

Figure 6: RESTC experimental results for hydrogen injected at inlet (ϕ_I = 0.15) and hydrocarbon fuel injected at the combustor injectors (ϕ_C = 0.6).

2.2 Cavity Engine Simulations

We performed both full RESTC engine and combustor portion simulations in this work to ascertain the extent of fuel-air mixing and to identify other interesting flow features that could not be gleaned from the experimental pressure measurements. These simulation results have been obtained very recently, and are currently still being analysed to extract further quantitative information. The full-engine simulations were performed for one case in order to provide flow conditions representative of processing by the inlet, which was then utilised as a "flux-copied", inflow boundary condition for the remaining simulations. The simulations were performed using US3D, developed by Candler's group [11] who are one of the main partners we collaborate with within the AFOSR supported research groups. The code solves the compressible-form of the Navier-Stokes equations, with second order inviscid fluxes being calculated using the modified Steger-Warming method, and the viscous flux gradients computed using weighted least square fits. The Spalart-Allmaras one-equation turbulence model (in its compressive form) is used with turbulent Schmidt and Prandtl numbers of 0.7 and 0.9, respectively. The NASA Lewis database is used for determining the species properties.

The structured grid was created using GridPro v6.5 and had 21.3 million cells. The majority of the cells are located around the injectors and the cavity flameholder. The spacing of cells adjacent to the wall was set to one micrometer on all combustor surfaces, resulting in a y+ lower than one on the majority of surfaces. The reattachment point of the shear layer on the cavity ramp and in the vicinity of the injector bow shock had higher values of y+, but these were still less than three. A grid convergence study was not completed as the results will be compared to experimental data at a later date. However, the grid used here is comparable to other grids we have used in the past for simulations in similar scramjet engines [12].

Fuel-off cases:

Figure 7 shows the simulation results as contours of Mach number, temperature and density on select cross-section planes from the rectangular inlet to the combustor inlet. This clearly shows the shape-transition (from rectangular-to-elliptical) as well as the three-dimensional nature of the flow field. The density stratification of the flow entering the combustor, is an interesting feature that is common to most scramjet engines. This is usually difficult to obtain in experiments that utilize a direct-connect configuration to study the combustor in isolation, apart from also ingesting the facility boundary layer.

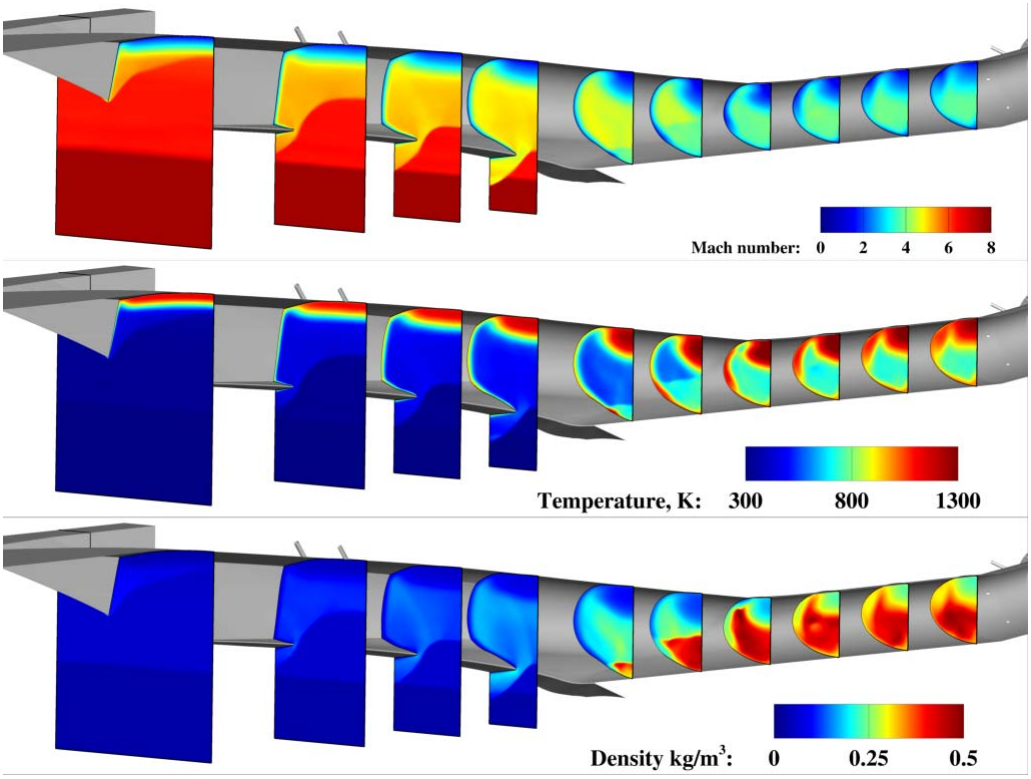

Figure 7: Cross-section planes along the flow direction from the inlet through to the combustor location of the RESTC engine showing filled contours of: Mach number, temperature and density.

The contour planes from which the fluxes are copied as an inflow boundary condition for the combustor and downstream flowpath are shown in Figure 8. This further demonstrates that the density field is highly stratified, and therefore care needs to be taken in tailoring fuel injection as well as the design of the cavity combustor in order to achieve the highest performance.

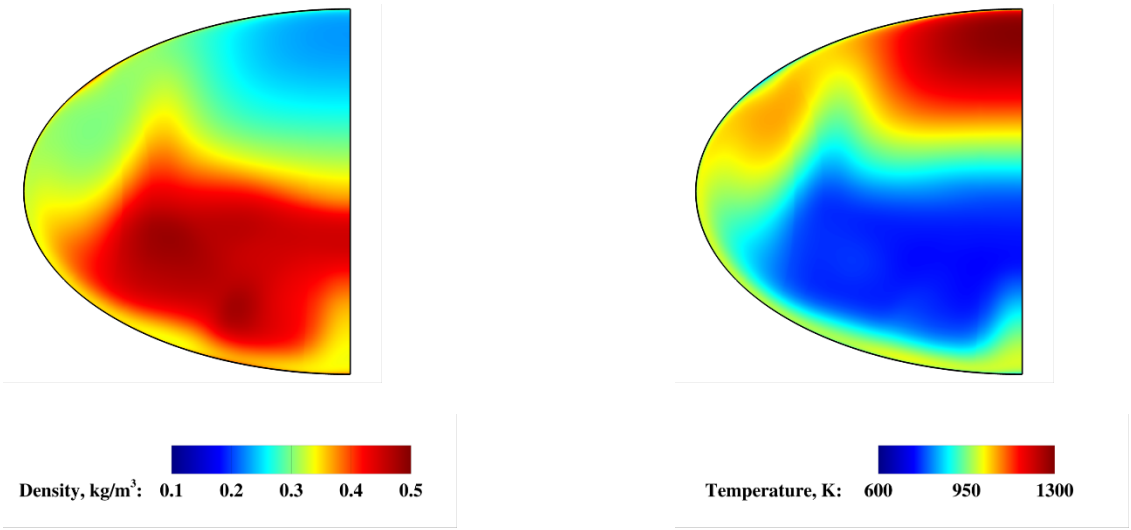

Figure 8: Cross-section planes of the location prior to the entry to the combustor used for the "flux-copied" boundary condition showing filled contours of density and temperature.

In this study only non-reacting flows were simulated, as the computational costs of the reacting hydrocarbon cases are beyond our current computing resources. The first comparison with the

experimental data for the fuel-off cases are presented in the figure below. It can be seen that both the full engine simulation (black solid line) as well as the flux-copied simulations (red dashed line) that only simulate the isolator, combustor and the downstream flowpath match the experimental data (black circles) very well for the body and the cowl sides. Therefore, the remaining simulations only employed the flux-copied approach to save computational costs by avoiding repeated simulations of the inlet flowpath.

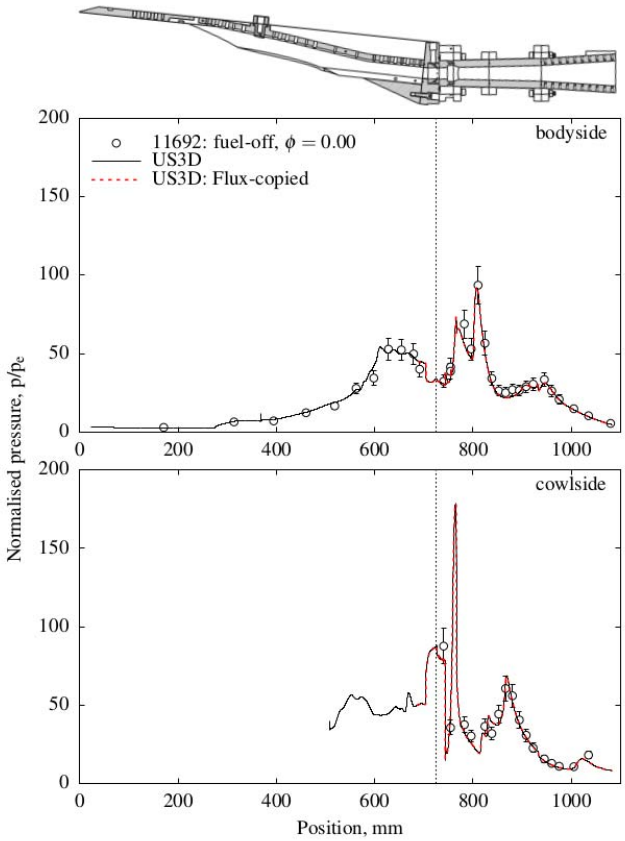

Figure 9: Comparison of US3D simulations of the full-engine and the abbreviated, flux-copied combustor and downstream flow path against the fuel-off experimental data.

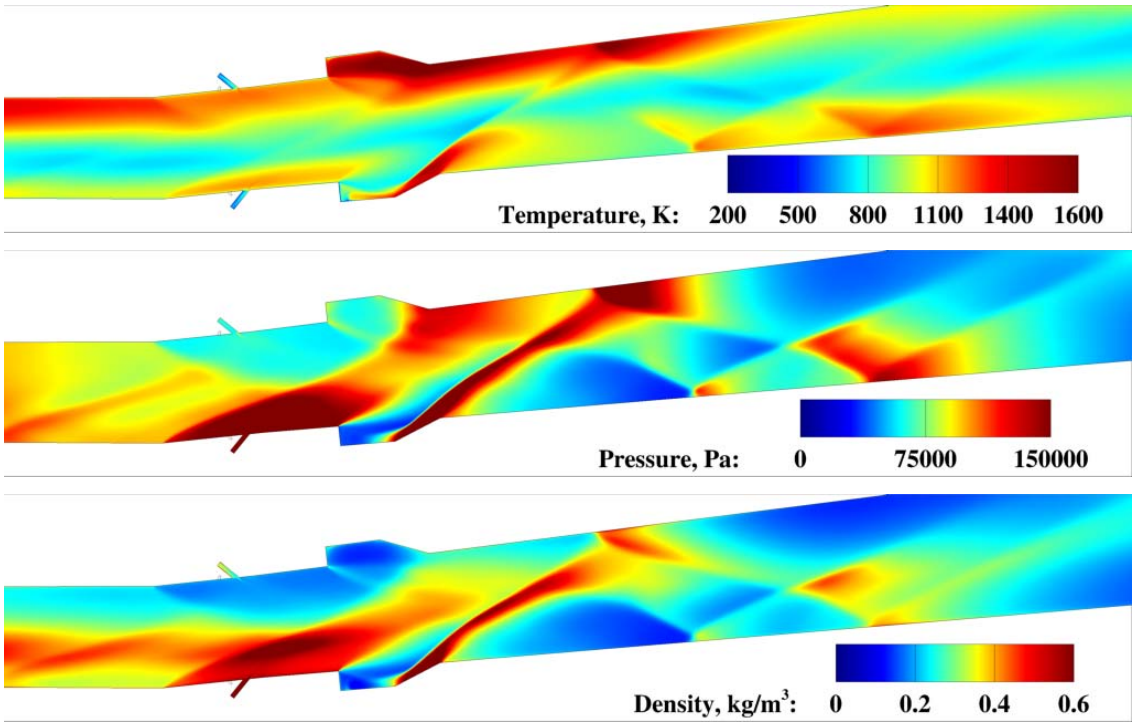

Figure 10: Filled contours of temperature, pressure and density of the plane of symmetry of the flow path from just upstream of the cavity combustor in the fuel-off case.

Figure 10 shows the complexity the flow owing to the internal shock structures around the cavity combustor region for the fuel-off simulation. These demonstrate that the body and cowl sides of the cavity combustor have very different flow conditions. The body side of the cavity has a higher temperature and pressure, while it is low on density compared to the cowl side. It should be borne in mind that the symmetry plane sliced contours only present a two-dimensional view, while there will be differences in the flow field with changing azimuthal angles. These can be seen by taking cross-plane contour slices perpendicular to the flow direction.

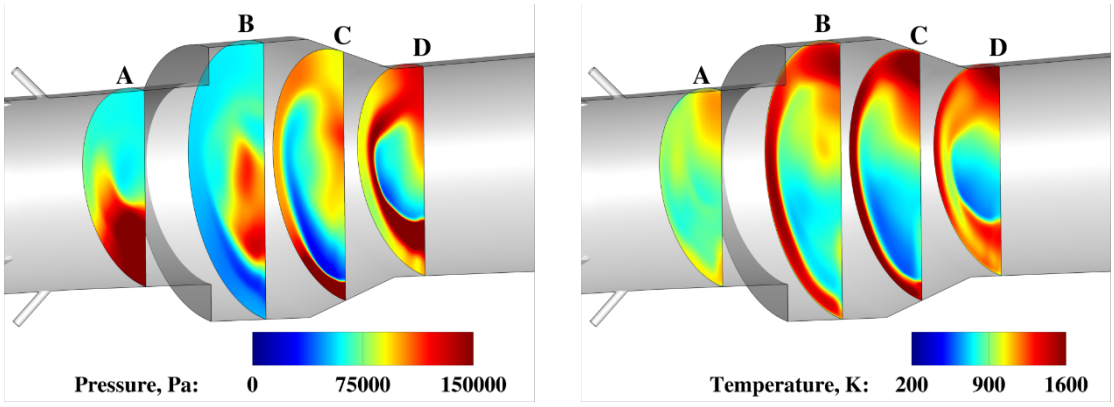

Figure 11: Filled contours of pressure and temperature at select cross-sections through the cavity combustor.

Figure 11 above shows such contour planes within the cavity combustor for pressure and temperature. Location A is just prior to the start of the cavity, B is in the flat but recessed portion, C is in the aft-ramp portion and D just outside the exit plane of the cavity. Owing to the sudden expansion following the step (start of the cavity) immediately after location A, the flow expands and has a lower

static pressure (see location B), however, the flow also slows down in the cavity leading to an increase in temperature throughout the circumference. As can be seen from the previous figure (Figure 10), a shockwave impinges on the start of the aft-ramp of the cavity on the cowl side, leading to higher pressure on the cowl side in location C. Owing to the ramp, further compression occurs at the body side that increases the pressure and temperature further into the core of the flow. On the cowl side, however, the flow has already turned along the ramp angle and experiences an expansion as it exits the cavity leading to a slight decrease in pressure near the wall, but with higher pressure where the shock reflected from the ramp passes the cross-section, as seen in location D. Therefore, the pressure and temperature distributions within the cavity is highly asymmetric and it can be expected that the flowfield within the cavity will be highly asymmetric as well. This can be seen very well from the streamlines traced within the cavity in Figure 12. In the symmetry plane view (left), it is seen that the bodyside of the cavity almost appears like a regular two-dimensional cavity as seen in many past studies [13]. However, the pressure imbalances within the cavity pushes the flow in the azimuthal direction leading to squiggly streamlines indicating that the flow swirls circumferentially within the cavity prior to exiting the cavity mid-way between the two injectors. This is a significantly different behaviour from the traditional two-dimensional cavities and presents options for future work targeting utilisation of the three-dimensional effects to increase residence time and improve fuel-air mixing.

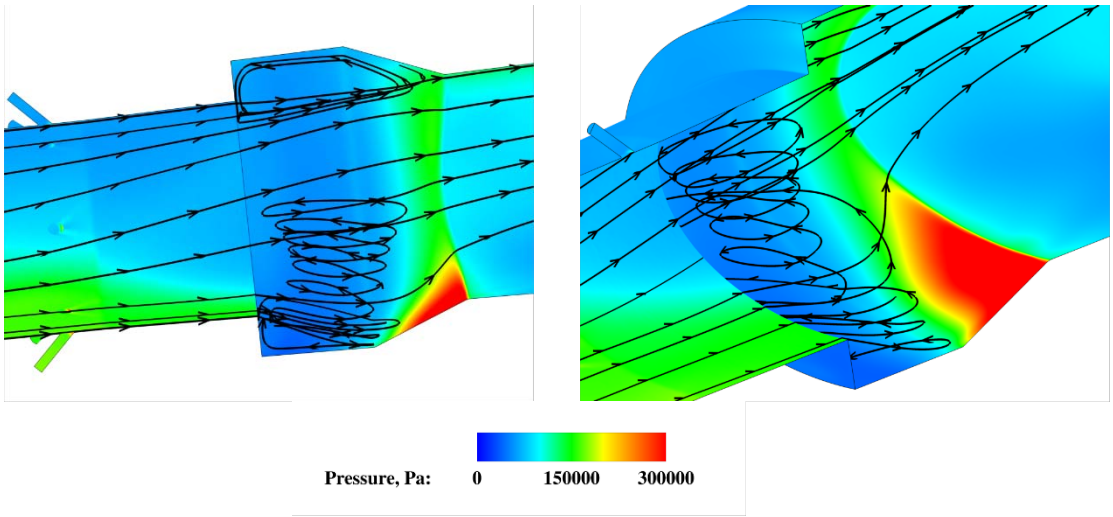

Figure 12: Streamlines within the RESTC cavity combustor.

Fuel-on mixing cases:

While the previous simulations shed light on the flow physics within the RESTC cavity combustor, it is important to bear in mind that these will be significantly altered when fuel is injected via the combustor injectors just prior to the start of the cavity. Figure 13 shows filled-contours of the equivalence ratio for methane and ethylene respectively at the engine's plane of symmetry. Again with the caveat that the two-dimensional image is only one slice of the full-engine, it can be seen that on the plane along which the injectors lie, the fuel is fully entrained into the cavity combustor and the cavity is in fact very fuel rich. The differences between methane and ethylene (as expected) are marginal and arise primarily owing to a small difference in their densities and mass-diffusion constants.

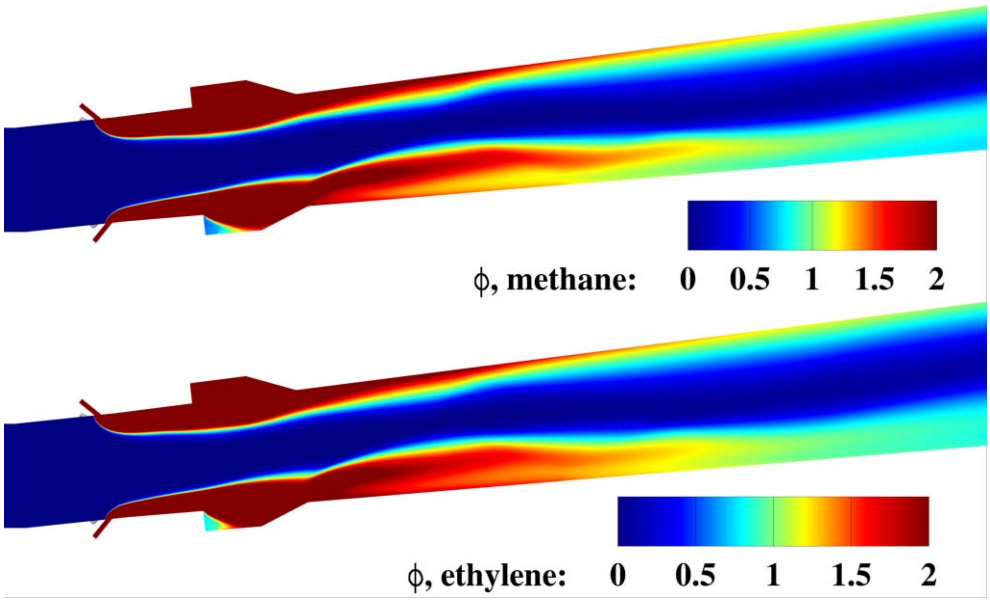

Figure 13: Filled contours of equivalence ratio for methane and ethylene injection into the cavity combustor along the engine's plane of symmetry.

As alluded to in the discussion of the previous figure, it can be seen through cross-section contours that are perpendicular to the flow direction (in Figure 14) in the cavity of equivalence ratio that the fuel injected is entrained in the cavity and experiences a highly three-dimensional processing within it. On the body side, owing to the lower density and pressure the fuel penetrates more into the core flow. The fuel blobs on the body side of the cavity merge together owing to the circumferential pressure forces acting upon them. The single fuel jet injected at the bottom of the cowl location remains isolated and does not mix with the other fuel blobs in the cavity, while the fuel injected between the body and cowl sides gets stretched and mixed within the cavity. Notably, there are very few locations with a stoichiometric composition and the cavity is predominantly stratified into rich and lean regions indicating that the mixing process is incomplete. Far downstream of the cavity, the region between the core of the flow and the wall of the engine has a significant region with an ignitable equivalence ratio.

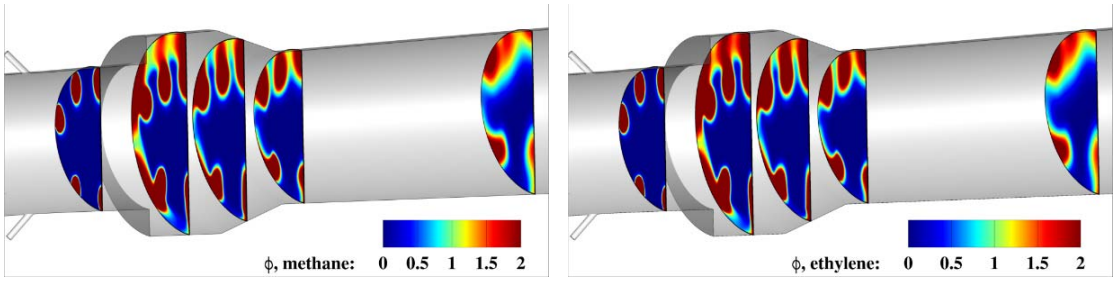

Figure 14: Filled contours of equivalence ratio for methane and ethylene injection into the cavity combustor along the engine's plane of symmetry.

While the contour plots indicate where stoichiometric mixtures are located in the cavity, in order to better understand the mechanisms responsible for ignition, it is important to understand how the fuel is entrained in the cavity, and how long it spends recirculating within the cavity. This will provide important clues about the residence time of the fuel-air mixture at conditions conducive to ignition. Streamlines of temperature and equivalence ratio for the case of methane injection is plotted in Figure

15. It can be seen that there is a small region between the body and cowl sides where recirculating flow is established that has an equivalence ratio around 1 and a suitably high temperature (above 800 K), that could be a potential location to initiate ignition. We are currently in the process of attempting to quantify the residence time from these simulations to have a more detailed understanding of whether the cavity can act as an ignition location.

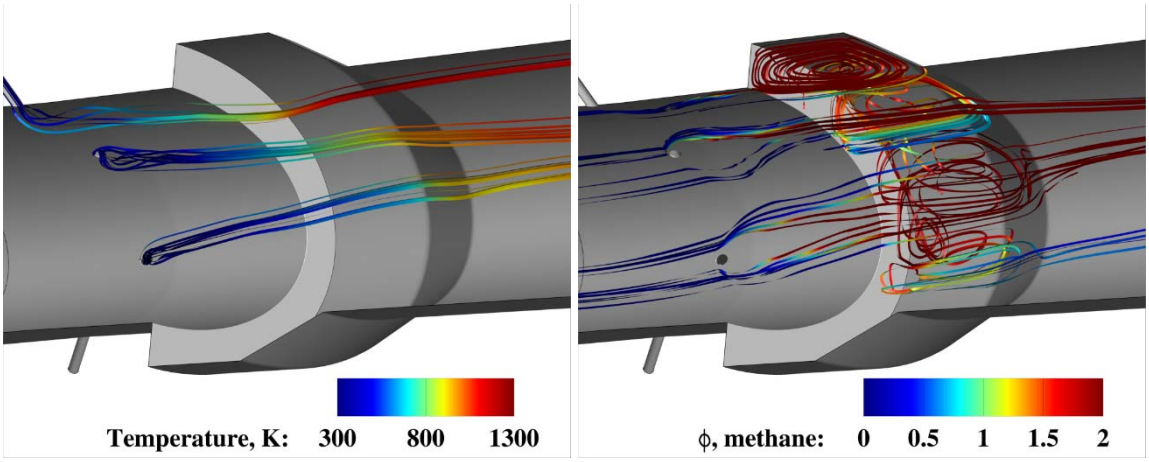

Figure 15: Filled contours of equivalence ratio for methane and ethylene injection into the cavity combustor along the engine's plane of symmetry.

3. Axisymmetric Experiments and mixing simulations

3.1 Design methodology and hardware

A view of the CAD representation of the axisymmetric model is shown in Fig. 16, and a cross-section view of the flowpath is shown in Fig. 17. This experiment is designed to examine hydrocarbon combustion and flame-holding at Mach 6-8 flight conditions. A Mach 4 facility nozzle is used to produce a 80 mm (~3.1 in) diameter core flow. The axisymmetric model consists of a diffuser (to reduce the flow to Mach 3), a 45 mm diameter constant area isolator, an injector block with angled porthole injectors, and a cavity around the circumference of the duct. Downstream of the cavity the combustor diverges to allow fuelling at high equivalence ratio.

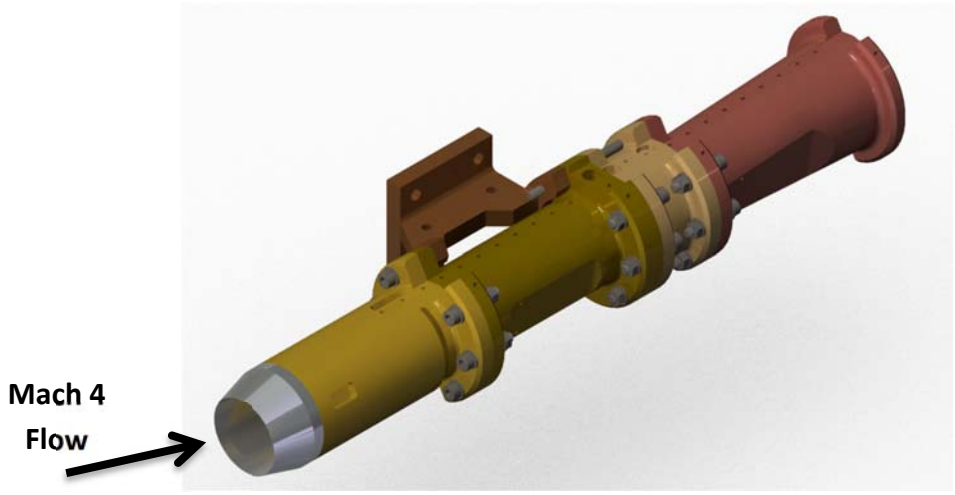

Figure 16 – Schematic of fundamental combustion experiment hardware

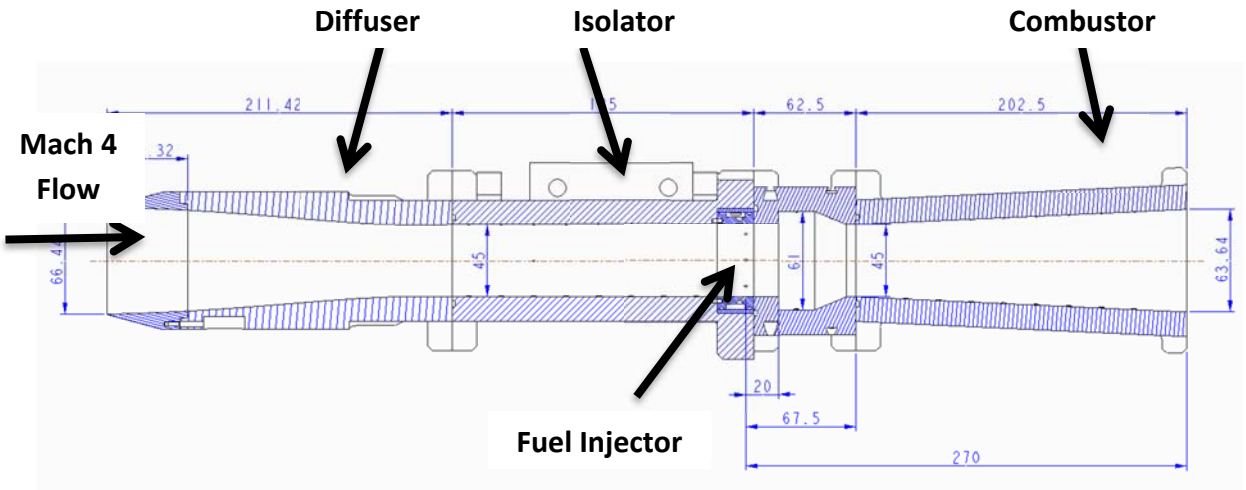

Figure 17 – Sectioned view of fundamental combustion experiment hardware

Testing of this model with unheated ethylene at Mach 8 conditions was conducted in the grant period. Figure 18 shows photographs of the axisymmetric model. It was manufactured in a modular style, so that different fuel injectors, cavities and combustors can be interchanged. The axisymmetric model consists of a diffuser (to reduce the flow to Mach 3), a 45 mm diameter constant area isolator,

an injector block with angled porthole injectors, and a cavity around the circumference of the duct. Downstream of the cavity the combustor diverges to allow fuelling at high equivalence ratio.

Figure 18 – Photographs of the axisymmetric scramjet combustor model

3.2 Optical Set-up

The Planar Laser-Induced Fluorescence (PLIF) technique was used to visualise the distribution of OH radicals in the model exhaust, as shown in 19. A laser sheet at a wavelength of 283.9 nm was used to excite OH radicals using the $Q_1(9.5)$-$Q_2(7.5)$ doublet in the (1,0) vibrational excitation band. The laser pulse energy was approximately 12 mJ each shot. Radicals then de-excite (fluoresce) producing emission that is then captured by a PIMAX 3 ICCD camera, filtered to capture emission within 310 ± 11 nm.

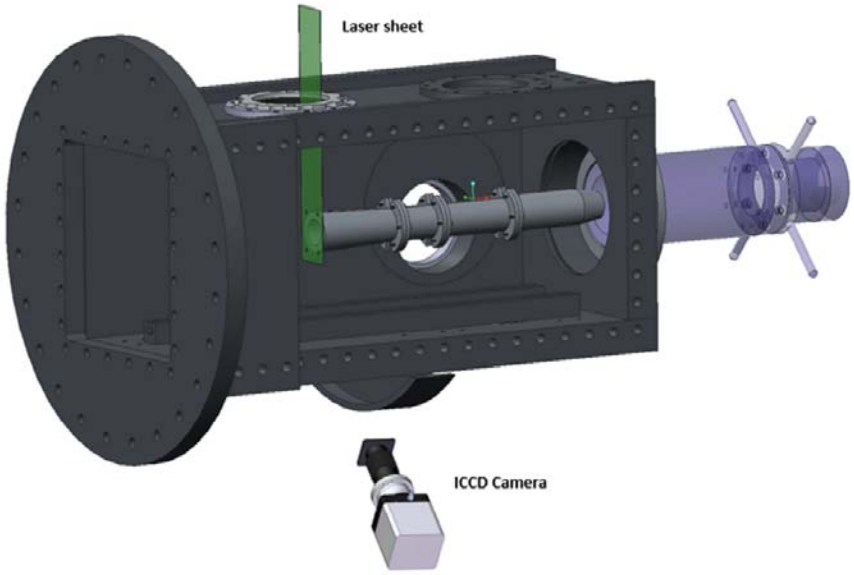

Figure 19. Optical arrangement for the OH PLIF technique, looking at rear of engine, flow from right to left.

The resulting fluorescence was normalised by the laser sheet intensity profile, then transformed spatially to compensate for the viewing angle of the camera. Since the imaging camera was not normal to the laser sheet, the image was distorted in an ellipse along the spanwise axis. Since the flow was axisymmetric, and no distortion was expected in the vertical direction, the streamwise axis was simply stretched to return the elliptical raw image to a circular exhaust profile. From this, the viewing angle of the camera was estimated to be $23°$, which agrees with the maximum viewing angle of $24°$ in Figure 20.

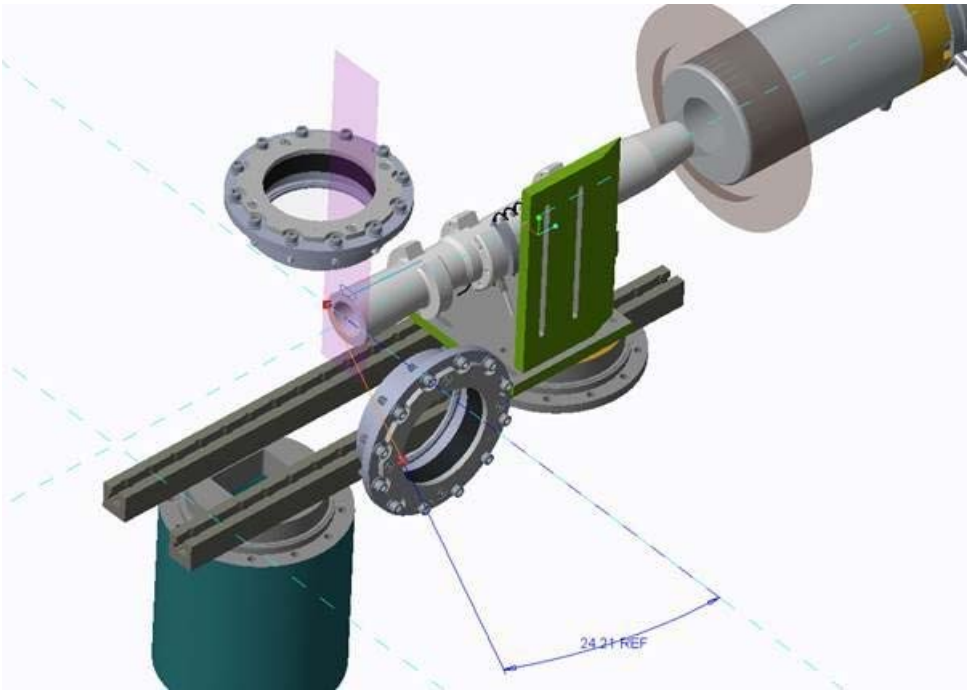

Figure 20. Maximum viewing angle through test section port. Looking at rear of engine, flow from top right to bottom left.

3.3 Test Condition

Experiments were tested in a "Cookie-cutter" configuration, where the diffuser entrance was placed within the core flow of the facility nozzle. This allowed the model to capture the majority of the nozzle test flow, whilst bleeding the nozzle boundary layer.

The freestream test conditions represented typical conditions expected for Mach 6-8, 50 kPa dynamic pressure flight condition, compressed to Mach 4 flow. The diffuser acted to further reduce the Mach number at the isolator entrance.

Two conditions were tested, designated as low enthalpy and high enthalpy respectively. The test condition properties from typical, representative shots are presented in Table 3.

Table 3. Typical Test Conditions

Quantity	Low Enthalpy	High Enthalpy	Unit
Shot Number	12046	12033	-
Stagnation Enthalpy	2.34	2.90	MJ/kg
Nozzle Supply Pressure	5.50	5.17	MPa
Static Pressure	33.7	32.8	kPa
Density	0.176	0.138	kg/m^3
Temperature	668	832	K
Streamwise Velocity	1980	2170	m/s
Mach Number	3.87	3.81	-

3.4 Pressure Measurements

Distributions of pressure are shown in Figures 21 and 22 for the two conditions. Each plot shows the distribution of pressure coefficient, C_P, defined as

$$C_P = \frac{P - P_e}{\frac{1}{2}\rho_e u_e^2}$$

Where P_e, ρ_e and u_e are the nozzle exit pressure, density and velocity respectively.

The following fuelling cases were tested:

1. Fuel-off, with air test gas.
2. Ethylene injection, with nitrogen test gas to supress combustion.
3. Ethylene injection, with air test gas, at a low equivalence ratio.
4. Ethylene injection, with air test gas, at a high equivalence ratio.

Comparison between fuelling cases 1 and 2 show the influence of increased mass flow rate through injection, as well as the influence of complex shock structures typical of porthole injection, with combustion chemistry suppressed by removal of oxygen from the freestream. Comparison between cases 2 and 3 therefore explicitly shows the influence of combustion, with case 4 providing insight of how increasing fuelling increases combustion-induced pressure rise.

The stagnation enthalpies and equivalence ratios for each condition in Figures 21 and 22 are presented in Tables 4 and 5, respectively. The maximum equivalence ratio of ER = 1 is used for nitrogen test gas case, as it presents the most conservative scenario when compared to fuel into air cases. There was no fuel into nitrogen case tested for the high enthalpy condition, so the low enthalpy fuel into nitrogen case was used in its place.

Table 4. Conditions for each low enthalpy fuelling case

Fuelling Case	Shot Number	Stagnation Enthalpy, MJ/kg	Equivalence Ratio
Fuel-off	12017	2.23	0.00
Fuel in N_2	12018	2.37	1.02
Fuel, Low ER	12048	2.36	0.14
Fuel, High ER	12049	2.36	0.29

Table5. Conditions for each high enthalpy fuelling case

Fuelling Case	Shot Number	Stagnation Enthalpy, MJ/kg	Equivalence Ratio
Fuel-off	12023	2.87	0.00
Fuel in N_2	12018	2.37	1.02
Fuel, Low ER	12033	2.90	0.39
Fuel, High ER	12040	2.93	0.59

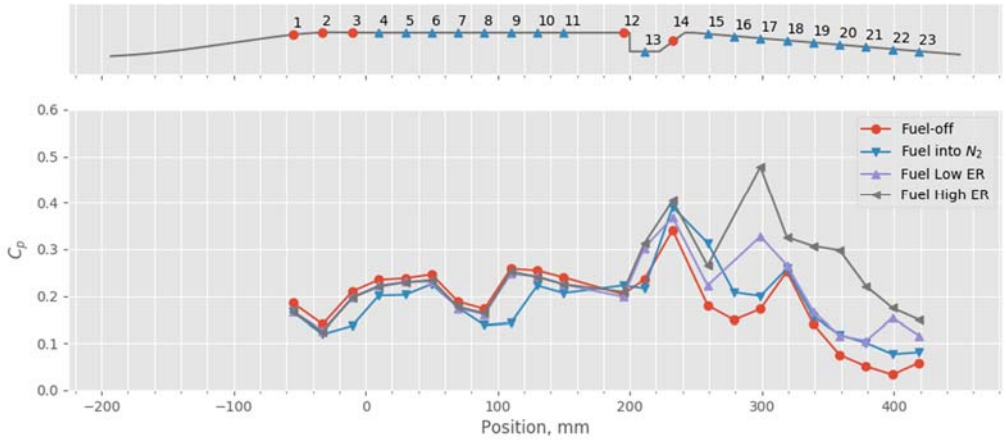

Figure 21. Pressure distribution for the low enthalpy condition

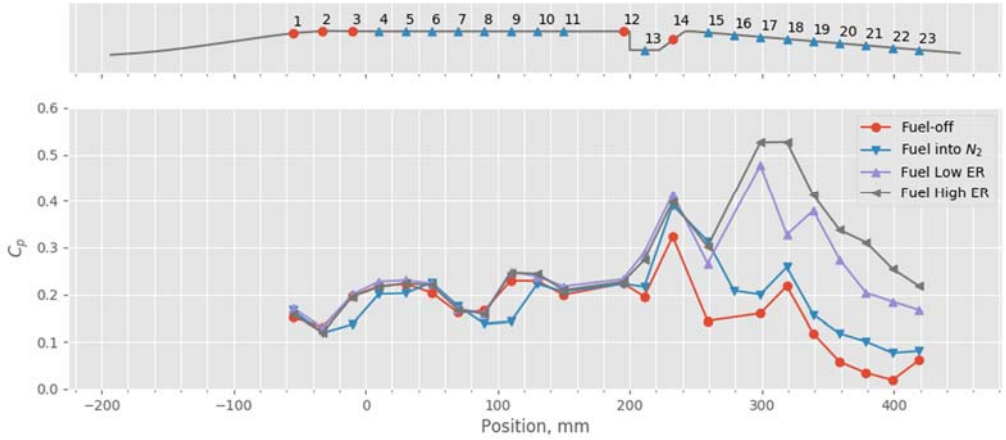

Figure 22. Pressure distribution for the high enthalpy condition

Figures 21 and 22 show the expected pressure distributions. All distributions are consistent prior to the injectors, indicating that the flow upstream is independent of fuel injection. There are some discrepancies for the nitrogen test case, as the different test gas changes the nozzle supply and nozzle exit conditions. Nonetheless, it acts as a useful comparison to the fuelled cases.

Downstream of the injectors, at approximately 185 mm, the injection characteristics increase pressure for all cases compared to the fuel-off case. Fuelled cases, both low and high equivalence ratio, show increased pressures relative to the nitrogen test gas case, indicating that combustion is occurring. Furthermore, increasing equivalence ratio (i.e. injecting more fuel) produces more combustion-induced pressure rise, indicating robust combustion. The low equivalence ratio, low enthalpy condition in Figure shows only marginal increases in pressure coefficient, indicating low levels of combustion. However, this is likely due to the very low equivalence ratio, ER = 0.14, used in this case.

3.5 OH Distribution

This section details the results from the OH PLIF imaging. As discussed previously, raw PLIF images were normalised by the laser sheet profile distribution.

The first set of images is shown in Figure 23. In order to facilitate comparison, each image is accompanied with its shot number, nozzle supply enthalpy and fuel-air equivalence ratio. The images have been cropped to emphasise the area of interest, being the exhaust of the scramjet combustor.

The exhaust of the engine is typically indicated by an outer dark circle of fuel-rich flow, an annular ring of OH within the reaction zone, then finally a dark core of fuel-lean air sits in the centre of each image. Surrounding each image is fluorescence from the freestream test gas that has passed around the combustor model. This freestream fluorescence is present regardless of the fuelling in the engine, but is eliminated when using a N_2 test gas, as in shot 12053 in Figure 24.

The images in Figure generally have low signal strength, except for shot 12035, which was much stronger. This shot had a stronger laser sheet profile, indicating that the laser was misaligned in the other shots. Additionally, the vertical dark line is an artefact from an artificially bright spot on the laser sheet profile caused by this misalignment. The laser was therefore realigned before further experiments, shown in Figures 25-26.

These PLIF images qualitatively show a number of interesting properties of the exhaust plume, including penetration into the core flow and turbulent length scales. As equivalence ratio is increased, the reaction zone penetrates further into the core flow, with a large dark band between the outer edge of the exhaust and the region of fluorescence. Shots 12041-12044 show repeats of the same condition, and the general structure of these images are quite similar, although the ring has become quite distorted in shot 12044. Shot 12045 shows a dual-mode condition, where the ring-like structure has almost completely broken down.

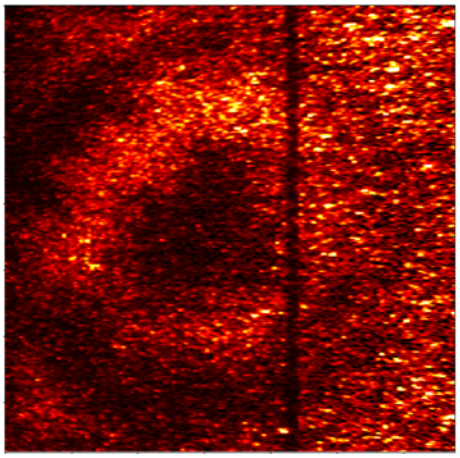

12034, 2.90 MJ/kg, ER=0.38

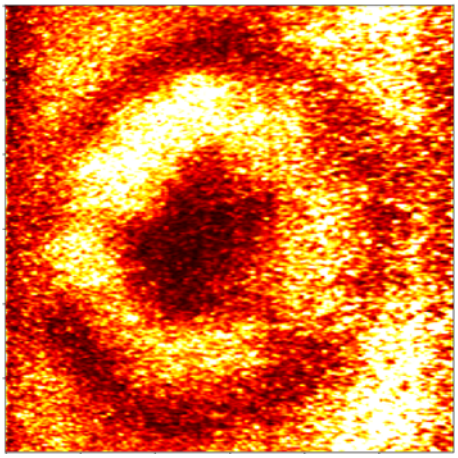

12035, 2.91 MJ/kg, ER=0.39

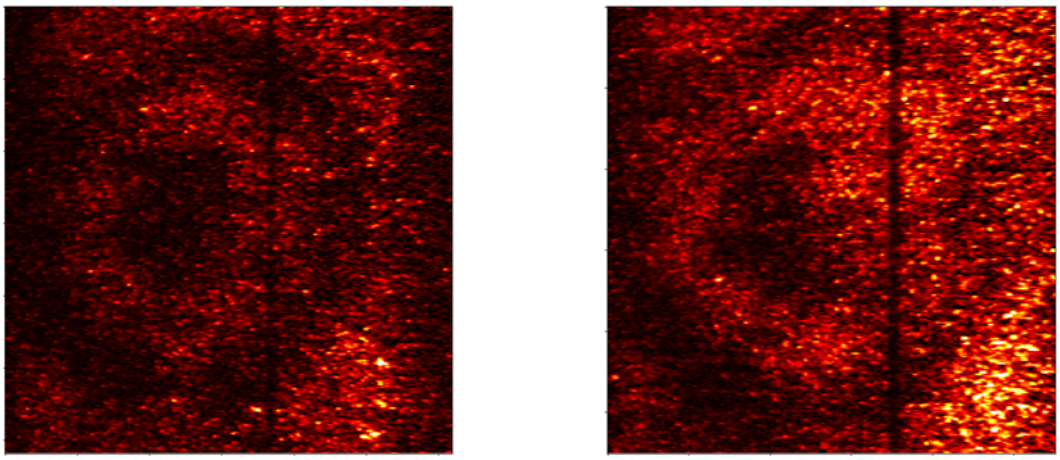

12037, 2.83 MJ/kg, ER=0.51 12039, 2.82 MJ/kg, ER=0.39

Figure23. Initial PLIF images, labelled with shot number, nozzle supply enthalpy and equivalence ratio.

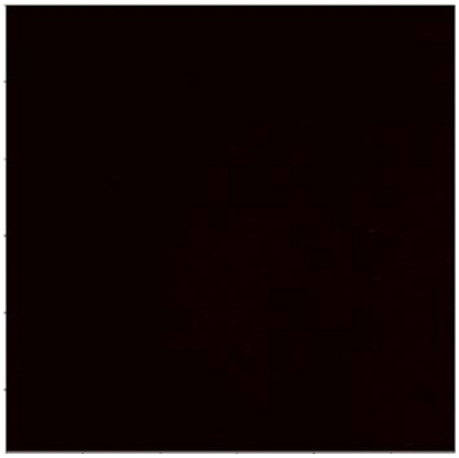

12053, 2.90 MJ/kg, ER=0.32

Figure24. Comparison PLIF image for Nitrogen test gas, labelled as in Figure.

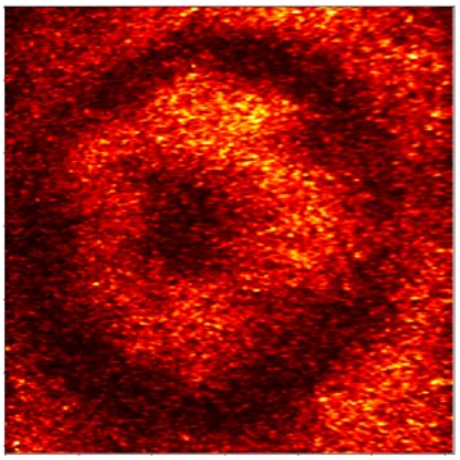

12040, 2.93 MJ/kg, ER=0.59

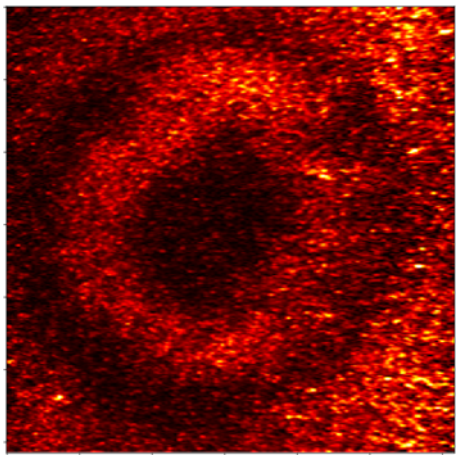

12041, 2.87 MJ/kg, ER=0.41

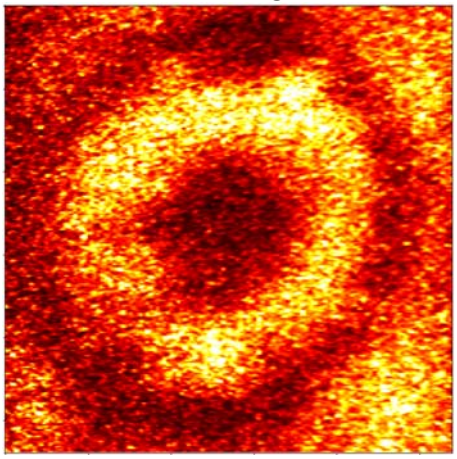

12042, 2.85 MJ/kg, ER=0.44

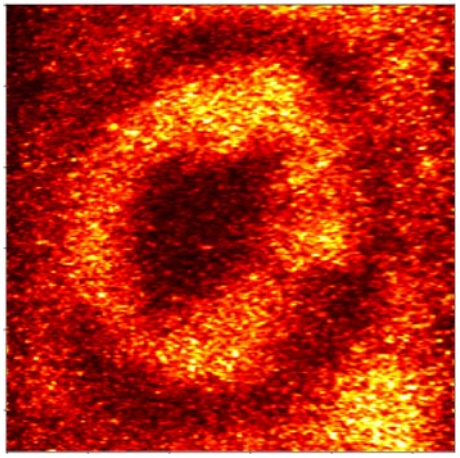

12043, 2.87 MJ/kg, ER=0.42

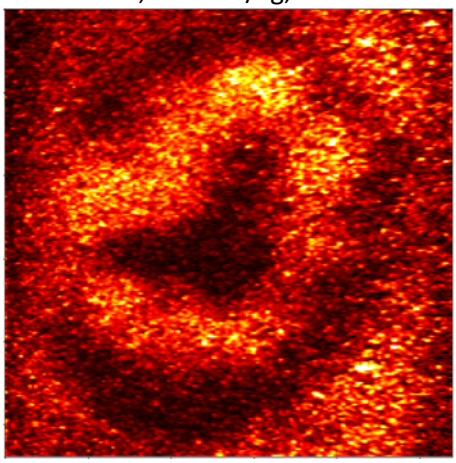

12044, 2.91 MJ/kg, ER=0.41

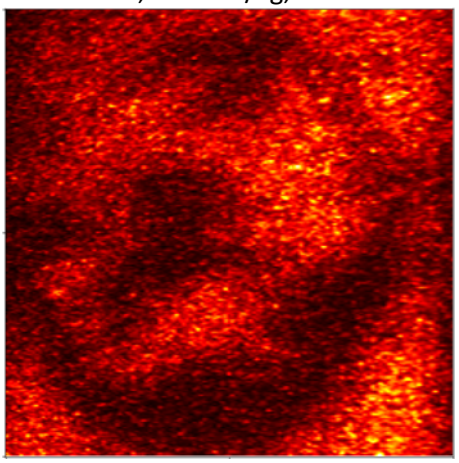

12045, 2.85 MJ/kg, ER=0.69 (Dual-mode)

Figure25. PLIF images, labelled as in Figure 23.

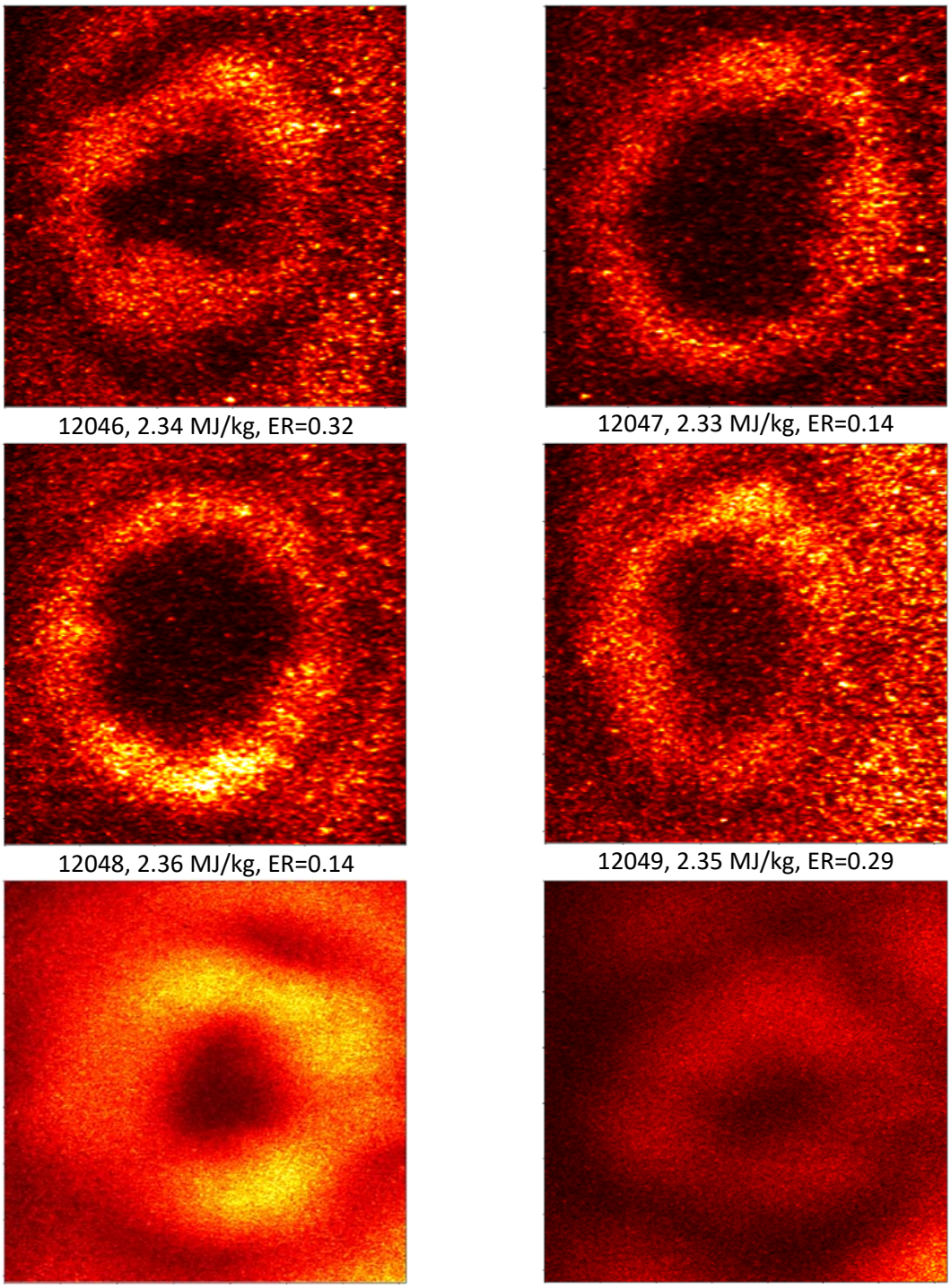

12046, 2.34 MJ/kg, ER=0.32

12047, 2.33 MJ/kg, ER=0.14

12048, 2.36 MJ/kg, ER=0.14

12049, 2.35 MJ/kg, ER=0.29

12051, 2.86 MJ/kg, ER=0.40

12052, 2.90 MJ/kg, ER=0.72 (Dual-mode)

Figure26. PLIF images, labelled as in Figure 23.

The low enthalpy condition is shown in shots 12046-12049. The low equivalence ratio condition has a remarkably different fluorescence profile, with OH seemingly attached to the wall of the combustor. As shown in Figure 21, this condition did not result in any significant combustion-induced pressure rise until $x = 400$ mm. It appears that, in the low equivalence ratio case, OH radicals are formed in the hot boundary layer, but recombination reactions do not reach completion. As such, there is no net release of heat, and no associated pressure rise.

Shots 12051 and 12052 show results with a larger magnification focussing lens on the imaging camera, however this made focussing worse and so was not pursued further.

3.6 Axisymmetric engine simulations

Non-reacting computations of the proposed axisymmetric combustor experiments were carried out to aid in their design. The goal of these simulations was to assess whether the combustor design (diffuser contraction ratio, cavity size, injector size and placement, fuel supply conditions and equivalence ratio) resulted in an acceptable distribution of fuel in the engine and conditions favourable for auto-ignition in the cavity. Simulations of the axisymmetric engine were conducted with UQ's in-house hypersonic flow solver Eilmer3 [14] using the k-ω turbulence model. The air and ethylene, which was taken as the representative fuel, were modelled as thermally perfect gases. Chemical reactions were not modelled.

To reduce computational costs, a separate axisymmetric Reynolds-averaged Navier-Stokes (RANS) simulation of the diffuser and combustor entrance (up to 25 mm upstream of the fuel injectors) was conducted. The air inflow conditions to the diffuser are taken to be those generated by the T4 Stalker Tube's Mach 4 nozzle operating at a stagnation enthalpy of 3.1 MJ/kg as detailed in the thesis of Ridings[15], which are given in Table 6 below. The free-stream turbulence intensity was taken to be 1%, and the corresponding laminar to turbulent viscosity ratio was taken to be unity. The effects of the simulated turbulence were suppressed until the empirical transition location at $Re_x = 2 \times 10^6$. The wall temperature was set to a constant value of 300 K to match shock tunnel experiments, and the grid is clustered towards the wall such that the height of the wall adjacent cell is approximately 1.7 wall units near the leading edge. The resulting converged static temperature field is shown in Figure 27. The outflow from this simulation is then mapped onto the inflow plane of a three-dimensional simulation of the remainder of the constant area combustor, including the fuel injectors.

Table 6: Axisymmetric engine test flow conditions in the T4 Stalker Tube

Velocity u_e (m/s)	Temperature T_e (K)	Pressure p_e (kPa)	Mach number M_e
2331	671	43.6	4.5

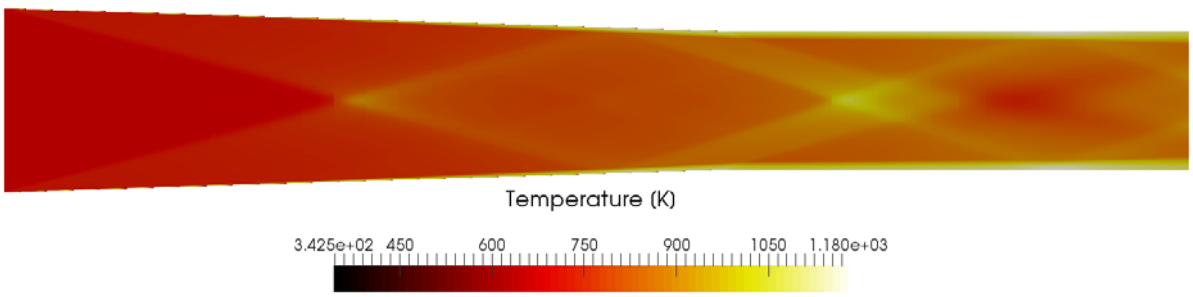

Figure 27: Simulated static temperature field in the diffuser and combustor entrance of the axisymmetric engine.

To simulate the fuel injection and mixing processes in the combustor, including the cavity, 3-D eilmer3 unsteady RANS (URANS) simulations of a sector of the combustor were undertaken. The sector extends from the centreline to the wall radially, from a jet centreplane to the symmetry plane between adjacent jets azimuthally, and from 25 mm upstream of the injectors to the exit of the constant area combustor axially. The resulting grid, generated with GridPro, is shown in Figure 28.

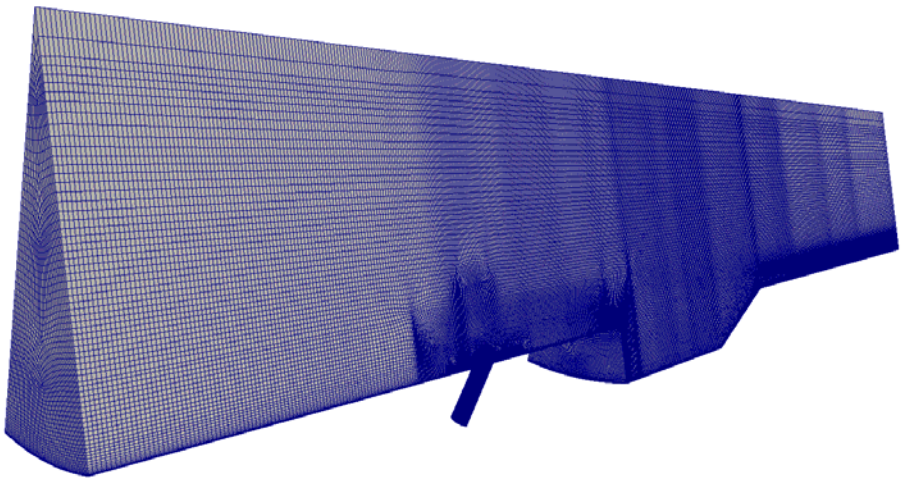

Figure 28: Grid for sector of the axisymmetric engine combustor.

As for the diffuser, a constant wall temperature of 300 K was used to replicate shock tunnel conditions. A number of different fuel supply conditions and injector sizes where simulated. It was determined that to achieve acceptable fuel penetration, the fuel plenum pressure had to be set to the maximum the T4 fuel system can deliver (3 MPa), and the injector size set to achieve an equivalence ratio of one. Only the results of this final fuelling configuration are presented here. In addition to the plenum pressure, a plenum temperature of 300 K was supplied to eilmer3's subsonic inflow condition at the end of the injector pipe. The URANS simulations were run up until $t = 200\ \mu s$, corresponding to approximately three flow-through times for the domain. Slices through the resulting distributions of fuel equivalence ratio and static temperature are shown in Figure 18. The top image shows the fuel distribution on the jet centerplane, which demonstrates that the fuel injectors achieve sufficient penetration bring the fuel into contact with the majority of the airflow. Beneath the distribution on the jet centerplane are five cross-planes, whose vertical edges are aligned with their axial location along the domain. Conditions within the cavity are shown at the bottom of the 2nd and 3rd cross-planes. These demonstrate that the fuel equivalence ratio in much of the cavity is order one, as desired for ignition. The corresponding temperature contours indicate that static temperatures of 1650 to 2000 K are achieved in the majority of the cavity. This exceeds what was achieved in the REST-C cavity, and is therefore favourable for the autoignition of at least ethylene.

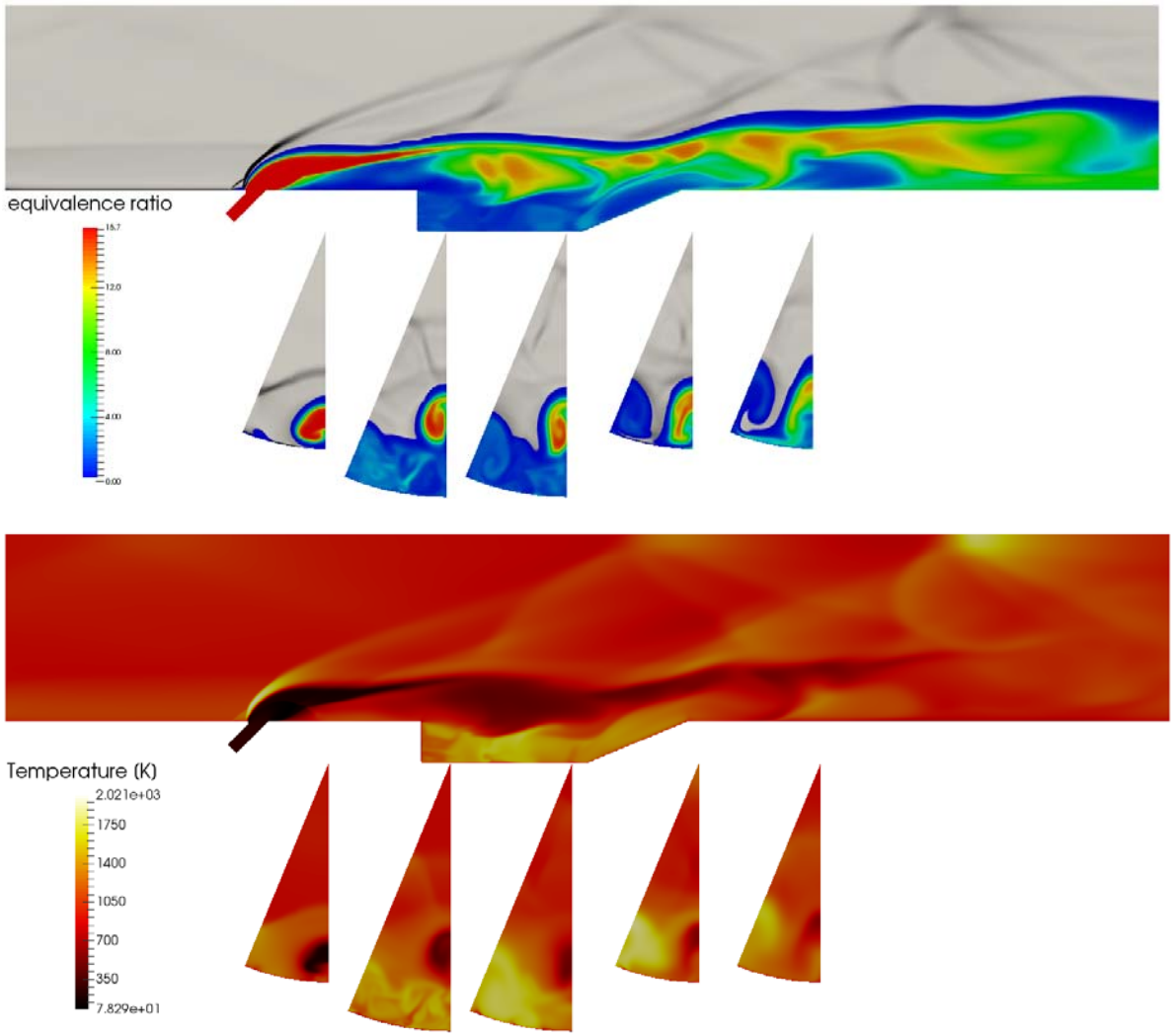

Figure 29: Injector centreplane and a series of cross-flow planes through the URANS solution of the combustor sector at $t = 200\ \mu s$. The top frame shows contours of fuel equivalence ratio in color (cut off at $\phi = 0.01$), overlaid on contours of temperature gradient magnitude in greyscale. The bottom image shows contours of static temperature.

References

[1] Z.J. Denman, W.Y.K. Chan, S. Brieschenk, A. Veeraragavan, V. Wheatley, M.K. Smart, Ignition Experiments of Hydrocarbons in a Mach 8 Shape-Transitioning Scramjet Engine, Journal of Propulsion and Power, 32 (2016) 1462-1471.
[2] M.J. Lewis, Significance of fuel selection for hypersonic vehicle range, Journal of Propulsion and Power, 17 (2001) 1214-1221.
[3] S.R. Turns, An introduction to combustion. 2nd, Boston: M cGraw Hill, (2000).
[4] M.B. Colket, L.J. Spadaccini, Scramjet fuels autoignition study, Journal of Propulsion and Power, 17 (2001) 315-323.
[5] K.R. Jackson, M.R. Gruber, T.F. Barhorst, The HIFiRE flight 2 experiment: an overview and status update, AIAA Paper, 5029 (2009) 2009.
[6] R. Stalker, A. Paull, D. Mee, R. Morgan, P. Jacobs, Scramjets and shock tunnels—the Queensland experience, Progress in Aerospace Sciences, 41 (2005) 471-513.
[7] M. Smart, Design of three-dimensional hypersonic inlets with rectangular-to-elliptical shape transition, Journal of Propulsion and Power, 15 (1999) 408-416.
[8] M.K. Smart, E.G. Ruf, Free-jet testing of a REST scramjet at off-design conditions.

[9] Z.J. Denman, S. Brieschenk, A. Veeraragavan, V. Wheatley, M. Smart, Experimental Design of a Cavity Flameholder in a Mach 8 Shape-Transitioning Scramjet, in: 19th AIAA International Space Planes and Hypersonic Systems and Technologies Conference, American Institute of Aeronautics and Astronautics, 2014.
[10] Z.J. Denman, V. Wheatley, M.K. Smart, A. Veeraragavan, Supersonic combustion of hydrocarbons in a shape-transitioning hypersonic engine, Proceedings of the Combustion Institute.
[11] I. Nompelis, T.W. Drayna, G.V. Candler, Development of a hybrid unstructured implicit solver for the simulation of reacting flows over complex geometries, AIAA Paper, 2227 (2004) 2004.
[12] W.O. Landsberg, V. Wheatley, A. Veeraragavan, Characteristics of Cascaded Fuel Injectors Within an Accelerating Scramjet Combustor, AIAA Journal, 54 (2016) 3692-3700.
[13] M.R. Gruber, R.A. Baurle, T. Mathur, K.Y. Hsu, Fundamental Studies of Cavity-Based Flameholder Concepts for Supersonic Combustors, Journal of Propulsion and Power, 17 (2001) 146-153.
[14] R.J. Gollan, P.A. Jacobs, About the formulation, verification and validation of the hypersonic flow solver Eilmer, International Journal for Numerical Methods in Fluids, 73 (2013) 19-57.
[15] A.N. Ridings, Investigation of pre-combustion shock trains in a sramjet using a shock tunnel at Mach 8 flight conditions, (2015).